Article

Quantitative Analysis of the Waterline Method for Topographical Mapping of Tidal Flats: A Case Study in the Dongsha Sandbank, China

Yongxue Liu [1,*], Manchun Li [1,*], Minxi Zhou [1], Kang Yang [1] and Liang Mao [2]

[1] Jiangsu Provincial Key Laboratory of Geographic Information Science and Technology, Nanjing University, Nanjing, 210023, China; E-Mails: zhouminxi_103@hotmail.com (M.Z.); yangkangnju@gmail.com (K.Y.)

[2] Department of Geography, University of Florida, Gainesville, FL 32611, USA; E-Mails: liangmao@ufl.edu

* Author to whom correspondence should be addressed; E-Mails: yongxue@nju.edu.cn (Y.L.); manchun@nju.edu.cn (M.L.); Tel./Fax: +86-25-8968-1181 (Y.L.).

Abstract: Although the topography of tidal flats is important for understanding their evolution, the spatial and temporal sampling frequency of such data remains limited. The waterline method has the potential to retrieve past tidal flat topography by utilizing large archives of satellite images. This study performs a quantitative analysis of the relationship between the accuracy of tidal flat digital elevation models (DEMs) that are based on the waterline method and the factors that influence the DEMs. The three major conclusions of the study are as follows: (1) the coverage rate of the waterline points and the number of satellite images used to create the DEM are highly linearly correlated with the error of the resultant DEMs, and the former is more significant in indicating the accuracy of the resultant DEMs than the latter; (2) both the area and the slope of the tidal flats are linearly correlated with the error of the resultant DEMs; and (3) the availability analysis of the archived satellite images indicates that the waterline method can retrieve tidal flat terrains from the past forty years. The upper limit of the temporal resolution of the tidal flat DEM can be refined to within one year since 1993, to half a year since 2004 and to three months since 2009.

1. Introduction

Tidal flats (also known as intertidal zones) are areas between the mean high tide and the mean low tide lines [1]. They are important coastal geomorphologic systems that provide habitats for wildlife, resources for land reclamation and protection for the coast against extreme storm events [2,3]. However, tidal flats have been considered economically unimportant areas in the past, and knowledge of their past topography is limited by the poor accessibility and significant temporal dynamics of the tidal flats, technical and financial limitations and indifference. It is impossible to retrieve the tidal flat topography of the past few years or even decades by using ground surveys, ship-based echo-sounding, airborne stereo-photogrammetry, airborne light detection and ranging (LiDAR) or airborne interferometric synthetic aperture radar (INSAR) [4–7].

The widely used waterline method, which uses a time series of satellite images taken during different tidal periods to map the topography of a tidal flat, may be the only method with the potential to retrieve digital elevation models (DEMs) of tidal flats from the past, because of the massive number of archived satellite images taken by various types of satellites. Over the past forty years, numerous space-borne platforms with increasing spatial, temporal and spectral resolutions have been deployed by the public and private sectors. For example, the Landsat 1–5 and 7 satellite series acquired and archived more than 434 terabytes of satellite images from 1972 to 2003 [8]. Remotely-sensed images have been estimated to be acquired at the rate of several terabytes per day [9]. The large numbers of archived images that cover broad areas of the coasts provide sufficient data to map the topography of tidal flats [10–20]. However, little is known about the factors that control the accuracy of DEMs that are based on the waterline method, possibly due to the lack of the synchronous validation data and the low utilization of archived satellite images. The lack of such knowledge may hinder researchers in constructing, interpreting and applying tidal flat DEMs to understand the evolution of tidal flats. This study aims to close this knowledge gap and investigates the factors that influence the accuracy of DEMs that are based on the waterline method. The article is organized as follows. The second section introduces the study area, the Dongsha Sandbank, and the data collection process. The third section describes the rationale of the waterline method and the factors that potentially influence the results. In the fourth section, the correlation between the accuracy of the resultant DEMs and the influencing factors is quantitatively analyzed.
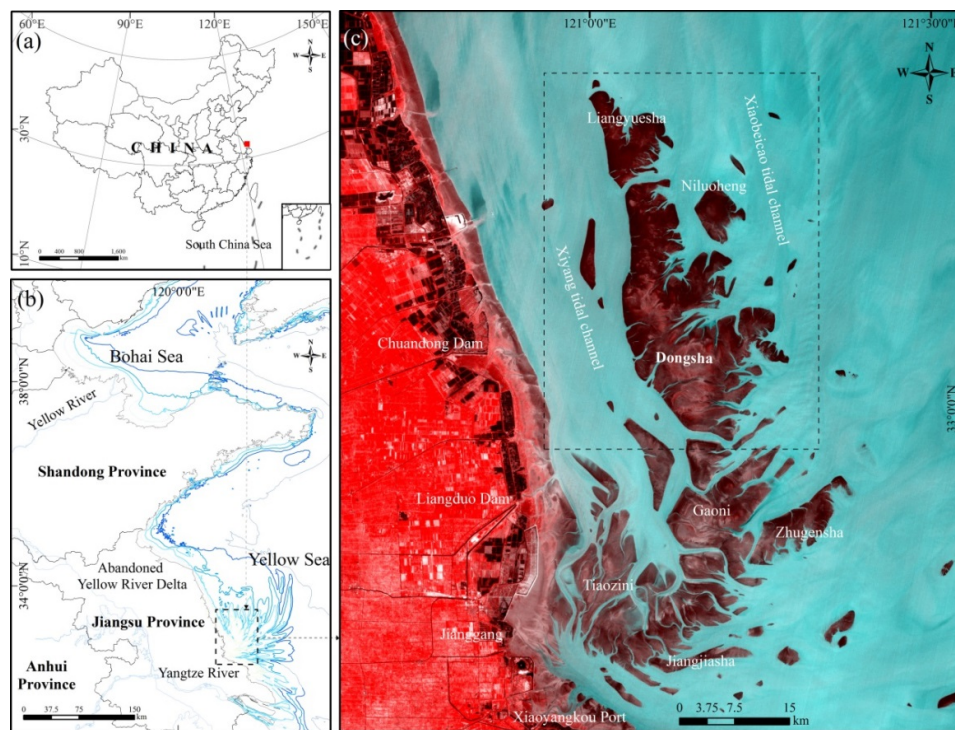
2. Study Area and Datasets

2.1. Study Area

The Dongsha Sandbank (Figure 1) is one of the largest offshore sandbanks in the South Yellow Sea Radial Sand Ridges (SYSRSR), which are the largest tidal sand ridges on the Chinese continental shelf [21]. The Dongsha Sandbank has an area of more than 1,267 km^2 above the sea chart datum [22,23]. The Dongsha Sandbank is a macro-tidal area with an average tidal range of 3.9–5.5 m and exhibits an irregular semi-diurnal tide [24]. During the high water periods, most of the Dongsha Sandbank is submerged under the sea [25]. In addition, the Dongsha Sandbank suffers significant erosion during tropical storms, which occur in the summer and autumn [26].

The Dongsha Sandbank was selected as a test site to explore the sensitivity of the waterline method for three reasons. First, Dongsha Sandbank is a large offshore tidal sandbank, and typical landforms (such as bare tidal flats, tidal ridges, tidal creeks and tidal basins) are well developed [22]. Second, almost all of the available high-quality medium-resolution satellite images (a total of 705 images) taken by various sensors from 1973 to 2012 have been collected and all of the available MODIS images have been collected. Third, other essential data from the Dongsha Sandbank, including hourly tidal gauge data from 1973 to 2012 and LiDAR DEMs measured in 2006, were collected by the research team.

Figure 1. Location maps of the Dongsha Sandbank (**a**) in China and (**b**) in the South Yellow Sea Radial Sand Ridges (SYSRSR); (**c**) HJ-1B Charge Coupled Device (CCD) false-color image of the study area using the near-infrared (band 4), red (band 3) and green spectral bands (band 2) mapped to RGB, acquired at Greenwich Mean Time (GMT) 02:36, 24 January 2010.

2.2. Datasets

The following materials were collected for the quantitative analysis of the waterline method:

(1) *Preview satellite images.* A total of 2,494 preview satellite images that cover the study area were collected. The images were taken from common civilian medium resolution satellite sensors, including the Landsat Multispectral Scanner System (MSS) [27], Thematic Mapper (TM) [28], Enhanced Thematic Mapper Plus (ETM+) [28], Japanese Marine Observation Satellite (MOS) [29], Multispectral Electronic Self-Scanning Radiometer (MESSR) [29], Japanese Earth Resources Satellite (JERS) [29], Synthetic Aperture Radar (SAR) [28], Indian Remote-Sensing Satellite (IRS) Linear Imaging Self-Scanning Sensor (LISS) and Advanced Wide-Field Sensor (AWiFS) [28], China-Brazil Earth Resources Satellite (CBERS) Charge Coupled Device (CCD) [30], Chinese Beijing-1 CCD and HJ CCD [31], European Remote-Sensing Satellite (ERS) SAR and the Environmental Satellite (Envisat)

Advanced Synthetic Aperture Radar (ASAR) [28]. Details of the image sources are listed in Table 1. Of all the preview images, 852 images are high-quality (cloud-free and containing clear waterlines).

Table 1. Summary of common satellite preview images. MOS, Marine Observation Satellite; JERS, Japanese Earth Resources Satellite; ERS, European Remote-Sensing Satellite; ESA, European Space Agency; CBERS, China-Brazil Earth Resources Satellite; IRS, Indian Remote-Sensing Satellite; CCD, Charge Coupled Device; MSS, Multispectral Scanner System; TM, Thematic Mapper; MESSR, Multispectral Electronic Self-Scanning Radiometer; SAR, Synthetic Aperture Radar; ETM+, Enhanced Thematic Mapper Plus; AWiFS, Advanced Wide-Field Sensor; ASAR, Advanced Synthetic Aperture Radar; CRESDA, Center for Resource Satellite Data and Applications.

Satellite	Sensor	Period	High-Quality	Total RS	Preview Images Source
Landsat-1/2/3/4 (USA)	MSS	1973–11 1998–12	136	294	JAXA, http://www.eorc.jaxa.jp [27]
Landsat-4/5 (USA)	TM	1984–05 2011–04	194	605	RSGS, http://www.rsgs.ac.cn [28]
MOS-1/1b (Japan)	MESSR	1987–09 1995–11	40	-	RESTEC, https://cross.restec.or.jp [29]
JERS-1 (Japan)	SAR	1992–10 1998–08	31	-	RESTEC, https://cross.restec.or.jp [29]
ERS-1/2 (ESA)	SAR	1995–12 2011–02	61	65	RSGS, http://www.rsgs.ac.cn [28]
Landsat-7 (USA)	ETM+	1999–10 2003–03	38	63	RSGS, http://www.rsgs.ac.cn [28]
CBERS01/02/02B	CCD	2000-09 2009–12	37	-	CRESDA, http://www.cresda.com [30]
IRS-P6 (India)	AWIFS	2005–02 2010–10	61	535	RSGS, http://www.rsgs.ac.cn [28]
Beijing-1 (China)	CCD	2006–03 2010–06	21	64	http://www.blmit.com.cn [31]
Envisat (ESA)	ASAR	2006–01 2010–12	55	-	RSGS, http://www.rsgs.ac.cn [28]
HJ-1 A/B CCD	CCD	2008–10 2010–12	178	705	CRESDA, http://www.cresda.com [30]

(2) *Medium spatial-resolution satellite images.* A total of 231 medium-resolution satellite images taken during different tidal periods in 1973–1977, 1980–1981, 1990–1991, 2000, 2006, 2007, 2008, 2009,and 2010 were obtained from several sensors, including Landsat MSS/TM/ETM+, MOS-1 MESSR, SPOT HRV, IRS-P6 LISS/AWiFS, CBERS-1/2 CCD, Beijing-1 CCD, HJ-1 A/B CCD, JERS SAR and ERS-1/2 SAR (Table 2). The spatial resolution of these satellite images varies from 10 m to 80 m. All the satellite images are of high-quality.

(3) *Airborne elevation data*. LiDAR data were collected in April and May 2006, by the Jiangsu Provincial Bureau of Surveying, Mapping and Geo-information. The LiDAR DEMs provided to the research team had a vertical accuracy of less than 15 cm and were resampled to a 5 m × 5 m grid.

3. The Rationale of the Waterline Method and Its Potential Errors

3.1. Rationale of the Waterline Method

Tidal flats are periodically flooded; hence, the boundaries of the exposed tidal flats (*i.e.*, waterlines) move back and forth as the tides rise and fall. The waterline method exploits the shifting waterlines that appear in the time-series satellite images as different quasi-contours of the tidal flat topography [12,32,33]. The heights of the waterlines can be measured from *in situ* data or marine hydraulic models. Hence, a tidal flat DEM can be generated by stacking a series of waterlines measured over a short period (Figure 2a). The following steps were commonly performed in sequence:

Table 2. Summary of the medium-resolution satellite images used in this study.

No.	Sensor	Acquisition Time[*] yyyy-mm-dd hh:mm	Height[†] (cm)	No.	Sensor	Acquisition Time[*] yyyy-mm-dd hh:mm	Height[†] (cm)	No.	Sensor	Acquisition Time[*] yyyy-mm-dd hh:mm	Height[†] (cm)
1	Landsat1 MSS	1973-11-16 02:01	−154.7	78	Landsat7 ETM+	2000-11-28 02:21	−2.3	155	IRS-P6 AWiFS	2008-03-24 02:46	4.9
2	Landsat2 MSS	1975-03-26 01:52	161.2	79	Landsat5 TM	2000-12-06 02:10	34.8	156	CBERS CCD	2008-04-23 03:07	36.9
3	Landsat2 MSS	1975-05-19 01:51	−78.5	80	Landsat7 ETM+	2000-12-14 02:21	−57.8	157	CBERS CCD	2008-05-02 02:55	88.9
4	Landsat2 MSS	1976-03-20 01:48	−230.7	81	Landsat5 TM	2000-12-22 02:10	116.7	158	CBERS CCD	2008-05-05 02:51	209.2
5	Landsat2 MSS	1976-04-07 01:47	−132.5	82	CBERS CCD	2006-01-10 02:35	21.3	159	IRS-P6 AWiFS	2008-05-06 02:53	177.8
6	Landsat2 MSS	1976-04-25 01:47	107.3	83	ERS SAR	2006-01-22 02:33	−132.5	160	IRS-P6 AWiFS	2008-05-07 02:33	63.7
7	Landsat2 MSS	1976-10-22 01:41	171.1	84	IRSP6 LISS3	2006-01-27 02:45	70.7	161	IRS-P6 AWiFS	2008-05-11 02:49	−184.3
8	Landsat2 MSS	1976-11-27 01:40	−170.8	85	IRSP6 AWiFS	2006-02-10 02:51	68.1	162	CBERS CCD	2008-05-31 02:52	68.0
9	Landsat2 MSS	1976-12-15 01:39	−48.2	86	ERS SAR	2006-02-26 02:33	122.0	163	CBERS CCD	2008-06-29 02:48	45.1
10	Landsat2 MSS	1977-04-02 01:35	127.9	87	CBERS CCD	2006-03-03 02:33	−96.7	164	CBERS CCD	2008-10-08 02:52	−7.1
11	Landsat2 MSS	1977-04-20 01:34	−89.7	88	CBERS CCD	2006-03-29 02:32	170.5	165	HJ-1B CCD	2008-10-17 02:43	70.7
12	Landsat3 MSS	1977-07-01 01:30	70.4	89	ERS-2 SAR	2006-04-02 02:33	−127.6	166	HJ-1A CCD	2008-10-27 02:50	191.9
13	Landsat2 MSS	1977-08-06 01:28	−121.9	90	BJ-1 CCD	2006-04-02 02:18	−155.2	167	HJ-1A CCD	2008-11-04 02:57	−61.4
14	Landsat2 MSS	1977-09-29 01:25	−71.4	91	ERS SAR	2006-04-17 14:14	−148.9	168	HJ-1A CCD	2008-11-12 03:03	176.7
15	Landsat2 MSS	1977-10-17 01:24	−189.4	92	CBERS CCD	2006-04-24 02:32	80.0	169	HJ-1B CCD	2008-11-21 02:45	−75.5
16	Landsat3 MSS	1980-05-01 01:45	−9.1	93	SPOT HRV	2006-05-03 02:30	−167	170	CBERS CCD	2008-11-29 02:52	82.4
17	Landsat3 MSS	1980-09-04 01:41	70.4	94	IRS-P6 LISS	2006-05-03 02:45	−155	171	HJ-1B CCD	2008-12-07 02:58	−57.5
18	Landsat3 MSS	1980-10-28 01:39	−184.9	95	ERS SAR	2006-05-07 02:33	−7.4	172	HJ-1B CCD	2008-12-10 02:36	103.3
19	Landsat3 MSS	1980-12-03 01:40	106.6	96	BJ-1 CCD	2006-05-21 02:21	−92.1	173	HJ-1A CCD	2008-12-12 02:38	155.6
20	Landsat2 MSS	1981-01-17 01:50	112.3	97	Landsat5 TM	2006-05-29 02:23	1.4	174	HJ-1B CCD	2008-12-14 02:39	83.8
21	Landsat2 MSS	1981-02-04 01:50	72.7	98	ERS SAR	2006-07-16 02:33	−193.2	175	HJ-1B CCD	2008-12-15 03:04	52.9
22	Landsat3 MSS	1981-04-26 01:45	−141.4	99	IRSP6 AWiFS	2006-07-29 02:33	−99.8	176	HJ-1A CCD	2008-12-16 02:41	−69.1
23	Landsat3 MSS	1981-06-01 01:47	177.6	100	SPOT HRV	2006-07-30 02:38	−121.3	177	HJ-1B CCD	2008-12-22 02:45	−23.0
24	Landsat3 MSS	1981-07-07 01:48	−197.9	101	BJ-1 CCD	2006-07-31 02:25	−138.5	178	HJ-1B CCD	2009-03-06 02:53	−79.3
25	Landsat3 MSS	1981-07-25 01:48	−59.5	102	Landsat5 TM	2006-08-01 02:23	−124.4	179	HJ-1B CCD	2009-03-14 02:59	−19.3
26	Landsat3 MSS	1981-08-12 01:49	117.0	103	ERS SAR	2006-08-20 02:33	123.1	180	HJ-1A CCD	2009-03-15 02:35	−132.9

Table 2. *Cont.*

No.	Sensor	Acquisition Time* yyyy-mm-dd hh:mm	Height† (cm)	No.	Sensor	Acquisition Time* yyyy-mm-dd hh:mm	Height† (cm)	No.	Sensor	Acquisition Time* yyyy-mm-dd hh:mm	Height† (cm)
27	Landsat2 MSS	1981-09-08 01:47	29.7	104	SPOT HRV	2006-09-06 02:35	197.7	181	HJ-1B CCD	2009-03-17 02:36	−168.3
28	Landsat3 MSS	1981-09-17 01:49	−135.6	105	Landsat5 TM	2006-09-18 02:24	116.6	182	HJ-1B CCD	2009-03-18 03:02	−139.0
29	Landsat3 MSS	1981-10-23 01:51	112.4	106	ERS SAR	2006-09-24 02:33	65.8	183	HJ-1A CCD	2009-03-20 03:03	−68.3
30	Landsat3 MSS	1981-11-10 01:51	178.2	107	Landsat5 TM	2006-10-04 02:24	159.5	184	HJ-1A CCD	2009-03-24 03:06	111.4
31	Landsat2 MSS	1981-11-19 01:48	−67.4	108	SPOT HRV	2006-10-06 02:31	217.8	185	HJ-1B CCD	2009-03-25 02:42	141.2
32	Landsat2 MSS	1981-12-07 01:49	84.5	109	BJ-1 CCD	2006-10-07 02:09	161.7	186	HJ-1B CCD	2009-04-02 02:48	−183.8
33	Landsat2 MSS	1981-12-25 01:49	87.1	110	IRSP6 AWiFS	2006-10-08 02:55	182.4	187	HJ-1B CCD	2009-04-06 02:51	79.4
34	Landsat5 TM	1990-02-26 01:51	7.2	111	Landsat5 TM	2006-10-20 02:24	170.2	188	HJ-1A CCD	2009-04-08 02:53	193.7
35	MOS1b MESSR	1990-04-05 02:29	10.6	112	IRSP6 AWiFS	2006-10-27 02:57	−34.4	189	HJ-1A CCD	2009-04-15 02:33	−144.7
36	MOS1b MESSR	1990-05-26 02:32	55.6	113	BJ-1 CCD	2006-10-29 02:10	−78.6	190	HJ-1B CCD	2009-04-17 02:35	−107.5
37	Landsat4 TM	1990-06-02 01:50	5.1	114	BJ-1 CCD	2006-11-01 02:30	61.0	191	HJ-1B CCD	2009-04-18 03:00	−77.0
38	MOS1b MESSR	1990-07-16 02:34	−102.9	115	SPOT-4 HRVIR	2006-11-01 02:31	64.8	192	HJ-1B CCD	2009-04-21 02:38	67.1
39	Landsat5 TM	1990-07-20 01:50	174.6	116	IRSP6 AWiFS	2006-11-02 02:33	122.8	193	HJ-1B CCD	2009-04-22 03:03	108.3
40	Landsat5 TM	1990-10-08 01:50	−125.2	117	BJ-1 CCD	2006-11-03 02:13	182.3	194	HJ-1B CCD	2009-04-25 02:41	167.7
41	MOS1b MESSR	1990-10-26 02:38	−54.0	118	IRSP6 AWiFS	2006-11-06 02:50	183.1	195	HJ-1A CCD	2009-04-27 02:42	49.7
42	MOS1b MESSR	1990-11-12 02:38	26.4	119	BJ-1 CCD	2006-11-15 02:04	56.0	196	HJ-1B CCD	2009-04-29 02:44	−117.2
43	MOS1 MESSR	1990-12-24 02:42	−140.0	120	ERS SAR	2006-12-03 02:33	159.0	197	HJ-1A CCD	2009-05-01 02:45	−187.7
44	MOS1 MESSR	1991-01-27 02:42	40.6	121	Landsat5 TM	2006-12-23 02:25	−25.9	198	HJ-1A CCD	2009-05-05 02:48	66.9
45	MOS1b MESSR	1991-02-05 02:41	−191.3	122	IRS-P6 AWiFS	2007-01-07 02:58	−59.6	199	HJ-1B CCD	2009-05-07 02:50	184.7
46	Landsat5 TM	1991-04-02 01:52	−128.5	123	CBERS CCD	2007-01-09 02:25	−155.9	200	HJ-1A CCD	2009-05-09 02:51	171.2
47	Landsat5 TM	1991-07-23 01:54	119.9	124	ERS2 SAR	2007-01-26 02:35	−186.2	201	HJ-1B CCD	2009-05-11 02:53	53.3
48	Landsat5 TM	1991-08-24 01:54	116.7	125	IRS-P6 AWiFS	2007-01-27 02:42	−141.9	202	HJ-1A CCD	2009-05-13 02:54	−66.6
49	MOS1b MESSR	1991-09-14 02:46	−108.6	126	IRS-P6 AWiFS	2007-01-31 02:58	98.6	203	HJ-1B CCD	2009-05-18 02:34	−55.9
50	MOS1b MESSR	1991-09-14 02:46	−108.6	127	IRS-P6 AWiFS	2007-03-11 02:46	−140.4	204	HJ-1B CCD	2009-05-22 02:36	154.6
51	Landsat5 TM	1991-10-11 01:54	−85.9	128	IRS-P6 AWiFS	2007-03-20 02:58	140.8	205	HJ-1A CCD	2009-05-24 02:37	183.4
52	MOS1b MESSR	1991-10-18 02:47	45.7	129	IRS-P6 AWiFS	2007-03-21 02:38	22.4	206	HJ-1B CCD	2009-05-26 02:39	68.6
53	Landsat5 TM	1991-11-28 01:54	−143.8	130	CBERS CCD	2007-03-28 02:22	−17.3	207	HJ-1B CCD	2009-12-03 02:52	136.1

Table 2. *Cont.*

No.	Sensor	Acquisition Time* yyyy-mm-dd hh:mm	Height† (cm)	No.	Sensor	Acquisition Time* yyyy-mm-dd hh:mm	Height† (cm)	No.	Sensor	Acquisition Time* yyyy-mm-dd hh:mm	Height† (cm)
54	Landsat7 ETM+	2000-01-29 02:23	−100.2	131	IRS-P6 LISS3	2007-04-04 02:47	64.2	208	HJ-1B CCD	2009-12-05 02:52	14.9
55	Landsat5 TM	2000-02-06 02:04	13.3	132	IRS-P6 LISS3	2007-04-09 02:43	−134.0	209	HJ-1B CCD	2009-12-07 02:55	−124.4
56	Landsat5 TM	2000-02-22 02:04	−109.3	133	IRS-P6 AWiFS	2007-04-13 02:59	1.3	210	HJ-1B CCD	2009-12-19 03:03	19.4
57	Landsat7 ETM+	2000-03-01 02:23	11.1	134	IRS-P6 AWiFS	2007-04-18 02:54	177.6	211	HJ-1A CCD	2009-12-20 02:38	−65.9
58	Landsat5 TM	2000-03-09 02:04	−124.1	135	IRS-P6 AWiFS	2007-04-23 02:50	−177.2	212	HJ-1A CCD	2009-12-21 03:03	−75.1
59	Landsat5 TM	2000-04-10 02:05	−215.7	136	IRS-P6 AWiFS	2007-05-08 02:37	−140.1	213	HJ-1B CCD	2009-12-22 02:41	−122.4
60	Landsat5 TM	2000-04-26 02:06	−109.1	137	ERS-2 SAR	2007-05-11 02:35	−67.4	214	CBERS CCD	2009-12-22 02:56	−111.9
61	Landsat5 ETM+	2000-05-04 02:23	144.5	138	CBERS CCD	2007-06-17 02:14	−28.0	215	ERS SAR	2009-12-27 02:35	−14.4
62	Landsat5 TM	2000-05-12 02:06	−56.4	139	ERS-2 SAR	2007-08-05 02:30	−177.3	216	HJ-1A CCD	2009-12-28 02:43	25.0
63	Landsat7 ETM+	2000-05-20 02:22	−5.8	140	IRS-P6 AWiFS	2007-09-04 02:42	−128.6	217	HJ-1B CCD	2009-12-30 02:46	111.9
64	Landsat5 TM	2000-05-28 02:06	8.2	141	ERS-2 SAR	2007-09-09 02:32	185.9	218	HJ-1A CCD	2010-01-01 02:46	133.5
65	Landsat7 ETM+	2000-06-05 02:22	−73.5	142	ERS-2 SAR	2007-10-14 02:30	9.2	219	HJ-1B CCD	2010-01-03 02:49	30.0
66	Landsat5 TM	2000-06-13 02:07	135	143	IRS-P6 LISS3	2007-11-06 02:46	120.8	220	HJ-1A CCD	2010-01-13 02:54	70.5
67	Landsat7 ETM+	2000-07-07 02:22	−207.7	144	IRSP6 AWiFS	2007-11-11 02:40	97.6	221	HJ-1B CCD	2010-01-14 02:32	112.3
68	Landsat5 TM	2000-07-31 02:08	134.7	145	IRS-P6 AWIFS	2007-11-21 02:32	97.9	222	Landsat5 TM	2010-01-16 02:22	95.6
69	Terra AST	2000-08-01 02:56	148.4	146	CBERS CCD	2007-11-28 02:00	−115.1	223	HJ-1B CCD	2010-01-18 02:34	11.5
70	Landsat5 TM	2000-09-01 02:08	−89.1	147	IRS-P6 LISS3	2007-11-30 02:45	−133.9	224	HJ-1A CCD	2010-01-24 02:36	−175.8
71	Landsat7 ETM+	2000-09-09 02:21	91.9	148	IRS-P6 AWiFS	2007-12-15 02:32	−122.7	225	HJ-1B CCD	2010-01-26 02:40	−92.5
72	CBERS CCD	2000-09-16 02:46	44.3	149	IRS-P6 AWiFS	2008-01-02 02:56	−68.5	226	HJ-1A CCD	2010-01-28 02:39	50.8
73	Landsat5 TM	2000-09-17 02:09	−92.6	150	IRS-P6 LISS3	2008-02-10 02:45	−47.2	227	HJ-1A CCD	2010-01-29 03:04	86.3
74	Landsat5 TM	2000-10-03 02:09	−142.7	151	CBERS CCD	2008-02-17 02:51	−12.4	228	ERS SAR	2010-01-31 02:35	60.2
75	Landsat5 TM	2000-11-04 02:09	−43.1	152	IRSP6 LISS3	2008-03-05 02:44	90.0	229	HJ-1A CCD	2010-02-05 02:44	−232.7
76	Landsat7 ETM+	2000-11-12 02:21	136.0	153	IRS-P6 AWiFS	2008-03-10 02:39	−11.5	230	HJ-1B CCD	2010-02-19 02:55	−103.7
77	Landsat5 TM	2000-11-20 02:09	−6.6	154	CBERS CCD	2008-03-14 02:51	−196.9	231	HJ-1A CCD	2010-02-21 02:54	−172.3

* The imaging moment is Greenwich Mean Time (GMT).

† Water level is at the Chenjiawu Tidal Gauge Station (datum: mean sea level).

(1) Extract the waterlines from the time-series of satellite images. The locations (*x, y*) of the water-land boundary are extracted from the satellite images.

(2) Simulate the water level at the time of satellite overpass. The water level (*h*) relative to a datum is calculated from transect data, tide gauge data or a hydraulic model.

(3) Assign a water level to each discrete waterline point. All of the waterlines are discretized to points and are then assigned water levels that correspond to the time of acquisition.

(4) Interpolate the tidal flat DEM. All of the waterline points over a specific period are merged into a waterline-point dataset, and a gridded DEM is created using spatial interpolation techniques.

All of the topographic maps hereinafter were generated using an identical, homogeneous processing methodology, described above.

Figure 2. (**a**) Diagram illustrating the waterline method; (**b**) potential errors in the waterline method. DEM, digital elevation model.
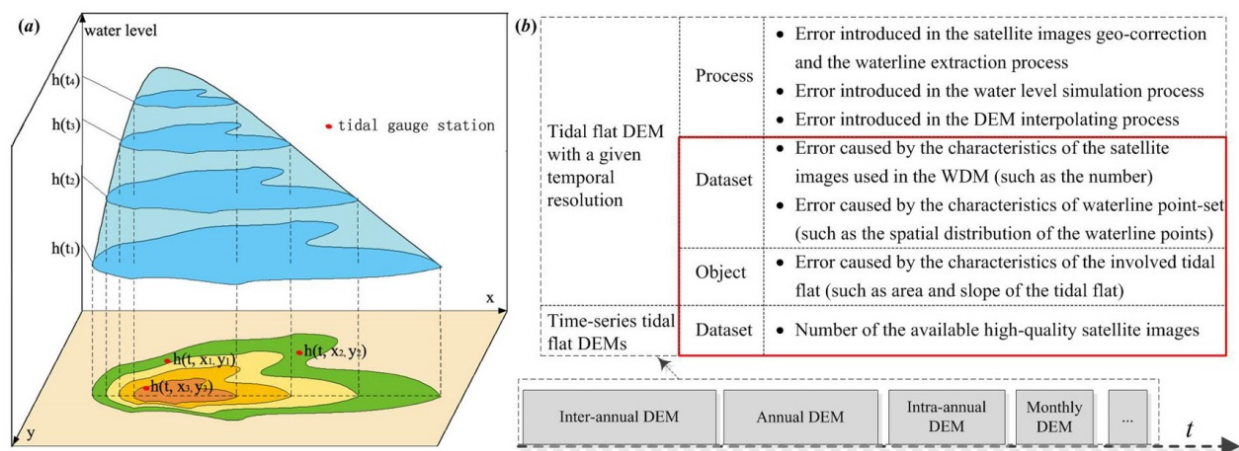
3.2. Potential Errors in the Waterline Method

The terrain of tidal flats is spatio-temporally dynamic due to variations in the tides, waves and other sedimentary factors [14]. The waterline method is proposed based on the following assumptions:

(1) a sufficient number of satellite images was taken over a short time period, so the variation in the topography over the tidal flats can be reasonably neglected [20];

(2) high-quality satellite images taken at various water levels were collected and can be used to construct a DEM over a given inter-tidal zone [19];

(3) the waterlines in a given satellite image accurately indicate the water level.

Hence, the errors in tidal flat DEMs lie not only in the planar dimension (*x, y*) and the vertical dimension (*z*), but also in the temporal dimension (*t*). Errors in tidal flat DEMs generated using the waterline method may be introduced at each stage and can be caused by the number of the satellite images used or the characteristics of the tidal flat (Figure 2b). The errors are summarized as follows:

(1) Positional error introduced during the geo-correction and waterline extraction processing of the satellite images. The error introduced in the geo-correction process may result in positional distortion of the waterlines in the satellite images. In most cases, the total root mean square error (RMSE) is less than 0.5 pixels because of the gentle topography in the intertidal zone [15]. Moreover, errors in the

positional accuracy may also arise from the waterline extraction process, in which the positional error depends on the waterline extraction method, the band combination, the influence of mixed pixels and other factors. The waterline position can easily be identified in the near-infrared or short-wave infrared bands [34]. Many waterline delineation methods have been proposed based on water's spectral characteristics in these two bands. However, it is difficult to find an appropriate method to delineate waterlines in multi-source and multi-temporal RS images. Moreover, the study region covers an area of more than 2,100 km^2, and the boundary between the water and the tidal flat varies spatially and temporally. To ensure the accuracy of the resultant tidal flat DEMs, on-screen digitization was used instead of automated waterline extraction methods. False-color composite (*i.e.*, near-infrared, red and green spectral bands) are preferred, because they best discern water from other land cover. Specifically, the near-infrared bands include band 4 of the Landsat TM, CBERS-2 CCD, HJ CCD, IRS-P6 and AWiFS/LISS images and band 3 of the SPOT HRV and Beijing-1 CCD images; the red bands include band 3 of the Landsat TM, CBERS-2 CCD, HJ CCD and IRS-P6 AWiFS/LISS images and band 2 of the SPOT HRV and Beijing-1 CCD images; and the green bands include band 2 of the Landsat TM, CBERS-2 CCD, HJ CCD and IRS-P6 AWiFS/LISS images and band 1 of the SPOT HRV and Beijing-1 CCD images. Digitization was performed according to the spectral and spatial characteristics of the tidal flats in the false-color composite images. Waterlines within the internal sandbank around tidal creeks were not considered in the analysis. The average positional error of the extracted waterlines is less than one pixel [17]. Given that the mean slope of a typical intertidal zone ranges between 1‰ and 3‰, the total positional error (1.5 pixels) may result in vertical errors of 4.5–13.5 cm on a 30 m resolution satellite image. Furthermore, the positional error introduced in the geo-correction and waterline extraction of the images and its influence on the accuracy has been discussed in the literature [20,32,35]; hence, this factor is not a focus of this study.

(2) Error introduced in the water level simulation process. The accuracy of the tidal level simulation depends on the complexity of the hydrodynamic conditions, the accuracy of the seafloor topography used in the hydrodynamic model, the characteristics of the simulation method (such as the cell size of the model and the open boundaries) and the accuracy of the calibration data [36]. The error is usually a few tens of centimeters (approximately 10–30 cm) under reasonably calm weather conditions [11,36]. In general, the waterlines can be treated as quasi-contour lines of the topography at a small scale. To apply the waterline method to broader regions, the spatial variation of the water level must be considered. This study covers an area of approximately 35 km × 60 km. A two-dimensional hydraulic model for the South Yellow Sea was constructed using Delft 3D (WL|Delft Hydraulics) to simulate the water level at the satellite overpass times. The average error in the tidal level simulation results is less than 30 cm [15]. Moreover, it is difficult to simulate the regional water level at different accuracies to analyze the relationship between the accuracy of the resultant tidal flat DEM and the accuracy of the water level simulation results. Hence, the vertical error caused by the hydrodynamic model was regarded as constant in the following quantitative error analysis.

(3) Error caused by the distribution of water levels. The distribution of water levels in the satellite images impacts the accuracy of tidal flat DEMs that are based on the waterline method. However, the tidal condition of the study area is complex; two tidal systems, the East China Sea progressive tidal wave and the Southern Yellow Sea rotary tidal wave, converge near the coastal waters of Jianggang [2]. The tide in the study region is not synchronous (especially on the eastern and western sides of the Dongsha

Sandbank), so it is difficult to analyze the distribution of the water level and its influence on the accuracy. Hence, the impacts of the distribution of water levels in the satellite images on the accuracy of the tidal flat DEMs are not fully considered in this study.

(4) Error introduced in the DEM interpolation process. This factor is analyzed in Section 4.1.

(5) Error caused by the number of time-series satellite images used in the waterline method. This factor is analyzed in Section 4.2.

(6) Error caused by the distribution of the water level. This factor is analyzed in Section 4.3.

(7) Error caused by the characteristics of the tidal flat (such as area and slope). This factor is analyzed in Section 4.4.

4. Quantitative Analysis Results

4.1. The Spatial Interpolation Approach and Its Impact on the Accuracy

The accuracy of the resultant DEMs depends on the spatial interpolation approaches that are used. This study used three spatial interpolation approaches, Inverse Distance Weighting (IDW), Ordinary Kriging (OK) and Thin Plate Spline (TPS), to generate three topographical maps of the Dongsha Sandbank (Figure 3a–c). These three approaches are integrated into the ArcGIS software (ESRI; http://www.esri.com). The waterline-point dataset was extracted from 40 images taken in 2006 (Table 2). In the IDW method, a variable search radius is adopted; the number of points used is set to 12, and the maximum distance is set at 1,000 m. In the OK method, a spherical model is used for the semi-variogram, and the same search strategy as in the IDW is used. In the TPS approach, the weight is set to 0.1, and the number of points used is set to 12.

> **Figure 3.** DEMs of the Dongsha Sandbank in 2006 from different approaches. (**a**) Interpolated using the Inverse Distance Weighting approach; (**b**) interpolated using the Ordinary Kriging approach; (**c**) interpolated using the Thin Plate Spline approach; (**d**) the light detection and ranging (LiDAR) DEM measured in 2006.
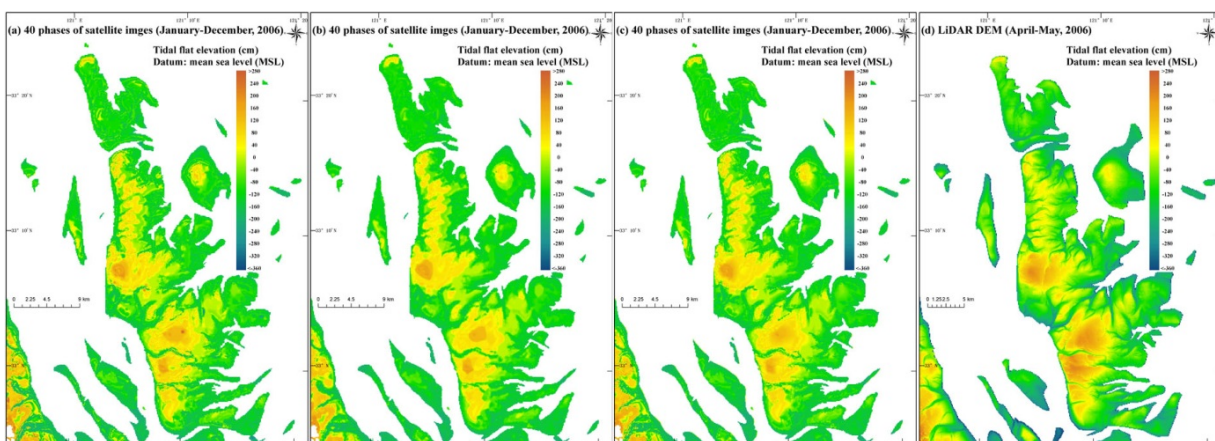
Few ground validation data are available, because of the large area and muddy surface of the tidal flats, the closely spaced tidal creeks and the complicated hydrodynamic conditions in the Dongsha Sandbank. Hence, a synchronous LiDAR DEM (Figure 3d) collected in 2006 (with a vertical accuracy of

less than 15 cm) was used as validation data. Error maps were obtained by subtracting the LiDAR-DEM from the three resultant tidal flat DEMs, and the RMSE of each of the error maps was calculated. The RMSEs of the resultant DEMs interpolated by the IDW, OK and TPS are 47.83, 45.27 and 44.79 cm, respectively. In this case, the TPS approach appears to have the best performance. Hence, in the following analysis, the resultant tidal flat DEMs are interpolated using the TPS approach.

4.2. The Number of Satellite Images Used and Its Impact on the Accuracy

The principle of the waterline method is to collect as many satellite images as possible that cover the study area over a given short time span, because the tidal conditions are different in almost all of the images. When a larger number of satellite images was used, more waterlines recorded at different water levels could be extracted, which resulted in more detailed topographical information. This section describes the quantitative analysis of the relationship between the number of high-quality satellite images and the accuracy of the resultant tidal flat DEM.

Forty satellite images taken in 2006 by different sensors were collected for this study (Table 2), and eleven tidal flat DEMs of the Dongsha Sandbank in 2006 (Figure 4a–k) were constructed based on different numbers of satellite images (from five to forty images). Figure 4a–k shows that the topographical information in the tidal flat DEMs is gradually refined, as additional satellite images are used in the waterline method compared with the synchronous LiDAR DEM (Figure 4l, measured in April and May 2006). The tidal flat DEM derived from five satellite images (Figure 4a) only represents general topographic information (especially on the ridge of the sandbank); in contrast, the DEM derived from twenty satellite images (Figure 4f) provides more details of the tidal flat topography (such as sand ridges and tidal creeks), and the DEM derived from forty satellite images (Figure 4k) offers even more detailed topographical information. Note that the tidal flat DEM derived from 32 satellite images (Figure 4i) is quite similar to the LiDAR DEM (Figure 4l).

The synchronous LiDAR DEM (Figure 4l) measured in 2006 was also used as validation data. Figure 5a shows the strong linear correlation between the number of satellite images used and the RMSEs of the resultant DEMs (R^2 = 0.9238, n = 11). In general, the RMSE of the resultant DEM decreases as the number of satellite images increases. For example, the RMSEs of the resultant DEM retrieved from five, twenty and forty satellite images are 62.43, 51.97 and 44.79 cm, respectively.

Note that the RMSE appears to reach a saturation point (45.44 cm) at 32 satellite images and then increases slightly as the number of satellite images increases. For example, comparing the two tidal flat DEMs in Figure 4i and j, although the number of satellite images increased by seven, the RMSE of the resultant DEM only decreased by 0.04 cm (blue ellipse in Figure 5a). The reason for this behavior will be analyzed in Section 4.3. In addition, previous studies have used different numbers of satellite images to map the tidal flat topography in different locations. In the literature, ten satellite images have usually been recognized as being sufficient [37,38]. In this case, the RMSE of the resultant DEM retrieved from twenty satellite images is 51.97 cm, even though twice as many satellite images were used as is generally considered sufficient. The high RMSEs may be due to the larger area of the study site (more than 620 km^2) than the areas investigated in other studies [37,38] and because the waterlines extracted from only ten satellite images do not completely cover our study site. A more detailed analysis will be presented in Section 4.4.

Figure 4. DEMs of the Dongsha Sandbank in 2006 constructed using different numbers of satellite images. (**a**) Five images in May; (**b**) nine images from April to May; (**c**) 13 images from April to July; (**d**) 15 images from April to autumn; (**e**) 17 images from March to autumn; (**f**) 20 images from March to September; (**g**) 22 images from February to September; (**h**) 29 images from February to October; (**i**) 32 images from January to October; (**j**) 39 images from January to November; (**k**) 40 images from January to December; and (**l**) LiDAR DEM measured in April and May.
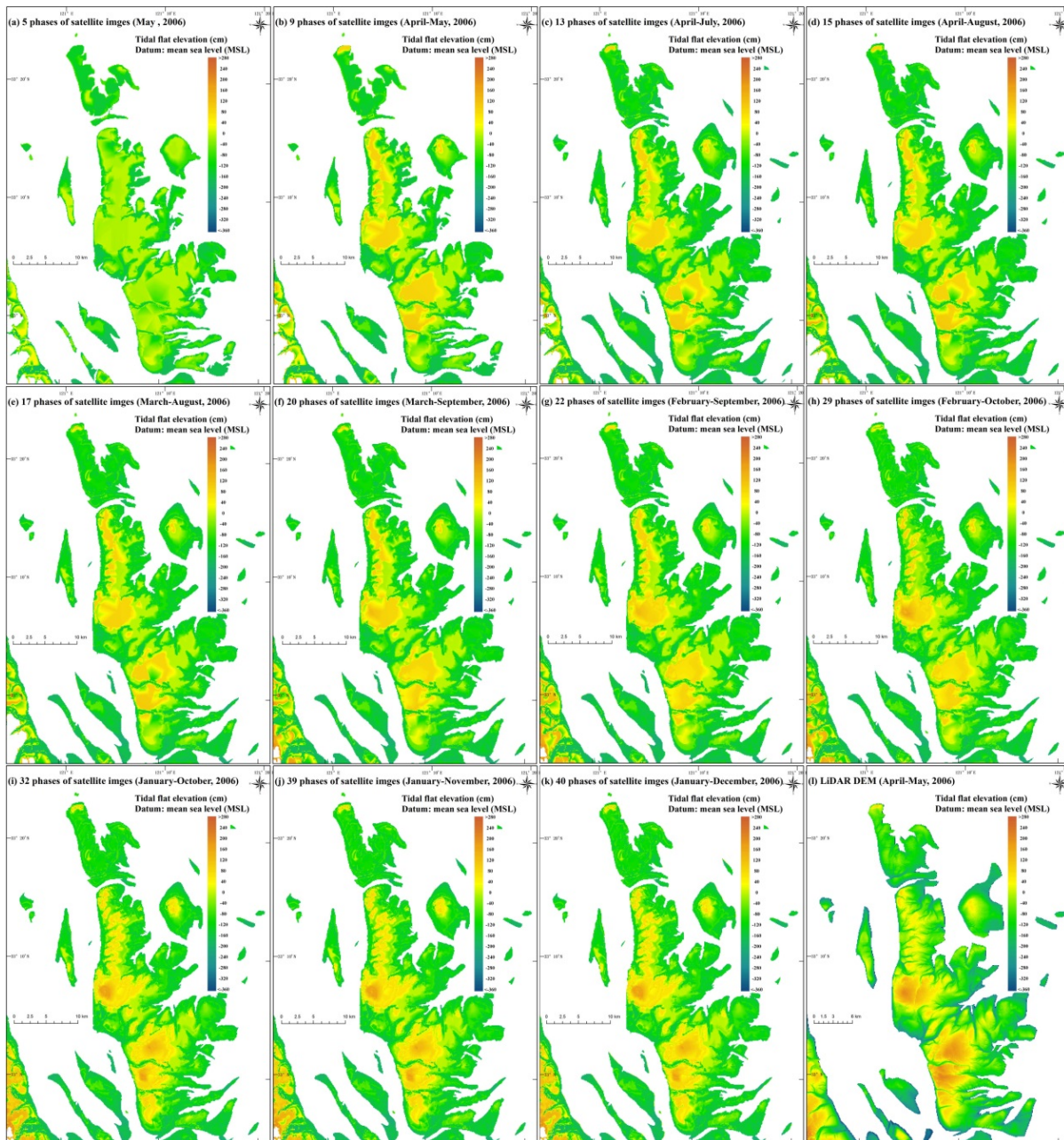
Figure 5. (**a**) Relationship between the number of satellite images used in the waterline method and the accuracy of the resultant DEMs; (**b**) relationship between the coverage rate of waterline points and the accuracy of the resultant DEMs.
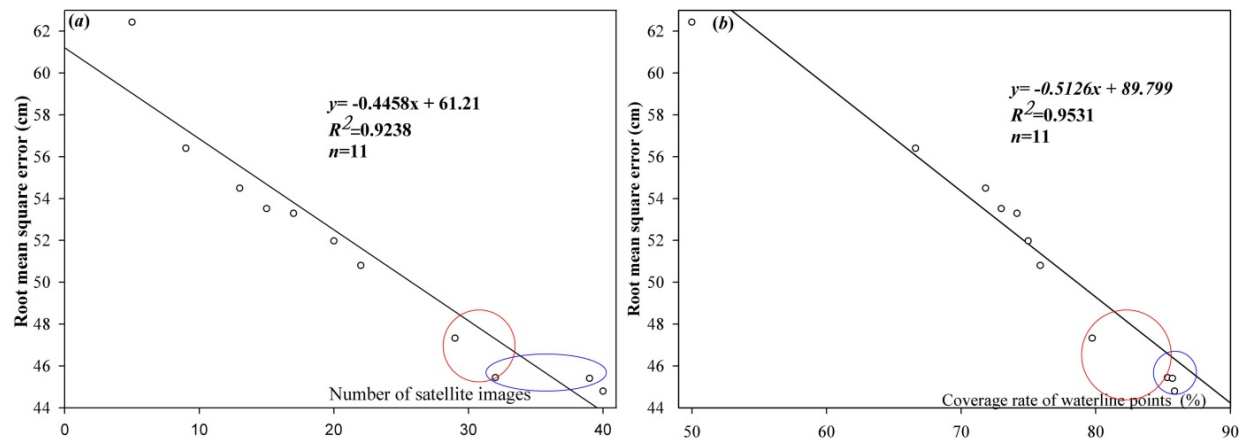
4.3. Characteristics of the Waterline Points and Their Impact on the Accuracy

In the construction of the gridded DEM, points with unknown elevations are interpolated from neighboring known points, and the regions of missing waterline points have an important influence on the interpolation. In general, the number of waterline points increases with the number of satellite images used. However, different parts of the tidal flat are submerged at different frequencies; the upper tidal flat is submerged less often than the lower tidal flat [17]. Hence, the density of waterline points may not increase in proportion to the number of satellite images; the additional waterline points from the additional satellite images may overlap each other in the commonly submerged areas and be sparse in the rarely submerged areas. In other words, after reaching the saturation point, the additional waterline points may be redundant and add few height measurements to the DEM construction process, even though more satellite images were used.

To validate this hypothesis, we converted the eleven waterline-point sets that were used to interpolate the eleven tidal flat DEMs in Figures 4a–k into raster format with a 60 m × 60 m cell size. If a cell has a corresponding height waterline point, the cell is labeled, and the proportion of labeled cells is calculated. Figure 5b shows a strong positive linear correlation between the RMSE of the resultant DEMs and the proportion of labeled cells (R^2 = 0.9531, n = 11). Specifically, Figure 4h was interpolated from 88,095 waterline points (a coverage rate of 79.73%) that were extracted from 29 satellite images (the red circle in Figure 5b), while Figure 4i was interpolated from 94,667 waterline points (a coverage rate of 85.32%) extracted from 32 satellite images (the red circle in Figure 5a). The 6,572 additional waterline points resulted in a 5.59% improvement in the coverage rate, which contributed to a 1.89 cm improvement in the performance of the DEM inversion (the red circle in Figure 5b). Although the number of satellite images used increased from 32 to 39 (the blue circle in Figure 5a), the accuracy only improved by 0.04 cm, which can be attributed to the small improvement in the coverage rate of only 0.53% (the blue circle in Figure 5b). Hence, the coverage rate of the labeled cells is more important to the improvement of the RMSE of the corresponding tidal DEMs than the number of satellite images. Moreover, according to the linear regression formula ($y = -0.5126x + 89.799$) derived from the eleven samples (Figure 5b), the

RMSE for a coverage rate of 100% will be 38.54 cm. This relationship may vary in different regions of the tidal flat. If the linear relationship can be determined in a given region, the coverage rate of waterline points may be used as an indicator to estimate the error of the tidal flat DEMs based on the waterline method when no validation data are available.

4.4. Characteristics of the Tidal Flats and Their Impact on the Accuracy

Mason [39] mapped tidal flat DEMs in tidal zones with different slopes and indicated that the vertical error of a tidal DEM is sensitive to the slope of the tidal flat. In the present study, an additional experiment was conducted to quantitatively explore the relationship between the accuracy and the slope. According to the LiDAR DEM measured in 2006, the maximum slope in the Dongsha Sandbank is 0.7 degrees (approximately 1:80 slope), the minimum slope is zero degrees, and the average slope is 0.1 degrees (approximately 1:550). We divided the LiDAR DEM into seventy levels according to the slope and calculated the RMSE of the tidal flat DEM derived from forty satellite images (Figure 4k) in the corresponding region. Figure 6a shows that there is a positive linear correlation ($R^2 = 0.7693$, n = 70) between the average slope of the tidal flat and the RMSE of the tidal flat DEM. In this case, the RMSE in the tidal flat area (slope < 0.2 degrees) is less than 55 cm, and the RMSE decreases to less than 45 cm in flatter tidal flat areas (slope < 0.1 degrees). Note that the tidal creeks and the neighboring regions usually have higher slopes; hence, a higher density of tidal creek systems may increase the error of the resultant tidal flat DEMs. In our case, the discrepancies along the tidal creeks are as high as 145 cm in some areas. Moreover, areas near the tidal creeks have higher mean absolute errors in the buffer area. Additional details about the tidal creeks and their influence on the accuracy of the resultant DEMs are discussed in the literature [17].

Figure 6. (**a**) Relationship between the error of the resultant DEMs and the slope of the tidal flat; (**b**) relationship between the area of the tidal flat and the accuracy of the resultant DEMs.
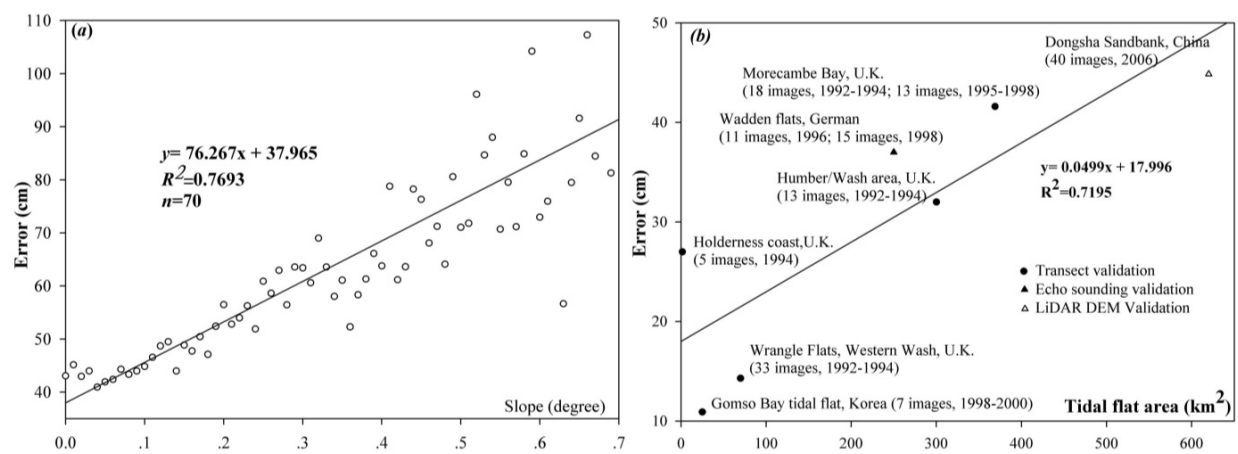
The waterline method has been successfully applied to many intertidal flat zones around the world, including the intertidal zones off the coast of England [7,11,18,40,41], the Wadden Sea tidal flat along the German coast [12], the Amazon-derived mud bank in French Guiana [13], the tidal flats along the

Korean coast [34] and the intertidal zones of the Chinese coast [20,42]. Of these studies, only seven provide the area and the accuracy of the mapped tidal flat. The area of the mapped tidal flats in the seven cases varied from 1.5 to 620 km^2, while the accuracy ranged from 14.0 to 44.79 cm. Figure 6b shows a positive linear correlation between area and accuracy (R^2 = 0.7195, n = 7), suggesting that the vertical errors of the tidal flat DEMs are positively correlated with the area of the region being studied. There are several possible explanations for this correlation. (1) The error in the resultant DEMs is sensitive to the spatial variability of the tidal flat. For instance, an ebb current in the tidal creek, which is supplied by the neighboring tidal flat surface and the upper reaches, has a significant impact on the morphological landscapes of the tidal flat. A larger catchment area of a tidal creek system will have a greater ebb discharge in the tidal creek and a more developed tidal creek system. A higher density of tidal creek systems may introduce additional errors in the tidal flat DEMs. (2) The difficult of constructing a hydraulic model increases as the area of the mapped tidal flat increases. The accuracy of the tidal flat DEMs depends on the performance of the hydraulic model, which depends on the data (such as the bathymetry data, the harmonic constant data at the open boundaries and the calibration data). Hence, it is difficult to build a hydrodynamic model associated with a larger tidal flat area and to maintain the accuracy of the water level simulation. Note that the relationship between the area of the mapped tidal flat and the error of the resultant tidal flat DEMs may be influenced by the different validation approaches (e.g., transect validation, echo sounding data validation and LiDAR DEM validation).

4.5. Potential Temporal Resolution of the Tidal Flat DEM Based on the Waterline Method

The terrain of tidal flats is spatio-temporally dynamic; hence, the temporal resolution of a given tidal flat DEM that is based on the waterline method is as important as the planar and vertical accuracies. The waterline method has not yet been developed to its full potential. To improve the accuracy of the waterline method, it is necessary to identify how rapidly and for how long to trace back the tidal flat terrains over the broad tidal flats.

A total of 852 high-quality satellite preview images of the study area were chosen based on a visual evaluation of the 2,494 preview images (Table 1). Of these high-quality preview images, 82.74% (*i.e.*, 705 images) were acquired by optical sensors, which is more than four times as many as those acquired by SAR sensors. A quarterly frequency analysis was conducted of all 852 high-quality preview images. Figure 7a shows the frequency distribution of the common satellite sensors from 1973 to 2011 at quarterly intervals. Since the launch of Landsat-1, the number of high-quality medium spatial resolution satellite images has increased gradually. Since 1984, a sufficient number of high-quality images (more than 20 images) that can be used to construct tidal flat DEMs have been collected every two years. Since 2006, a sufficient number of images (more than 40 images) have been collected each year, and since 2008, a sufficient number of images (approximately 20 images) have been collected every quarter, which is mainly attributed to the two-day revisit cycle of China's HJ-1A/B satellite.

Figure 7. Quarterly frequency of high-quality satellite images over the study area from 1973 to 2010. Please add subfigures caption in the caption. (**a**) Quarterly availability of high-quality satellite images based on the preview images taken by common satellite sensors; (**b**) Estimated quarterly availability of high-quality satellite images taken by all satellite sensors from 1973 to 2010.
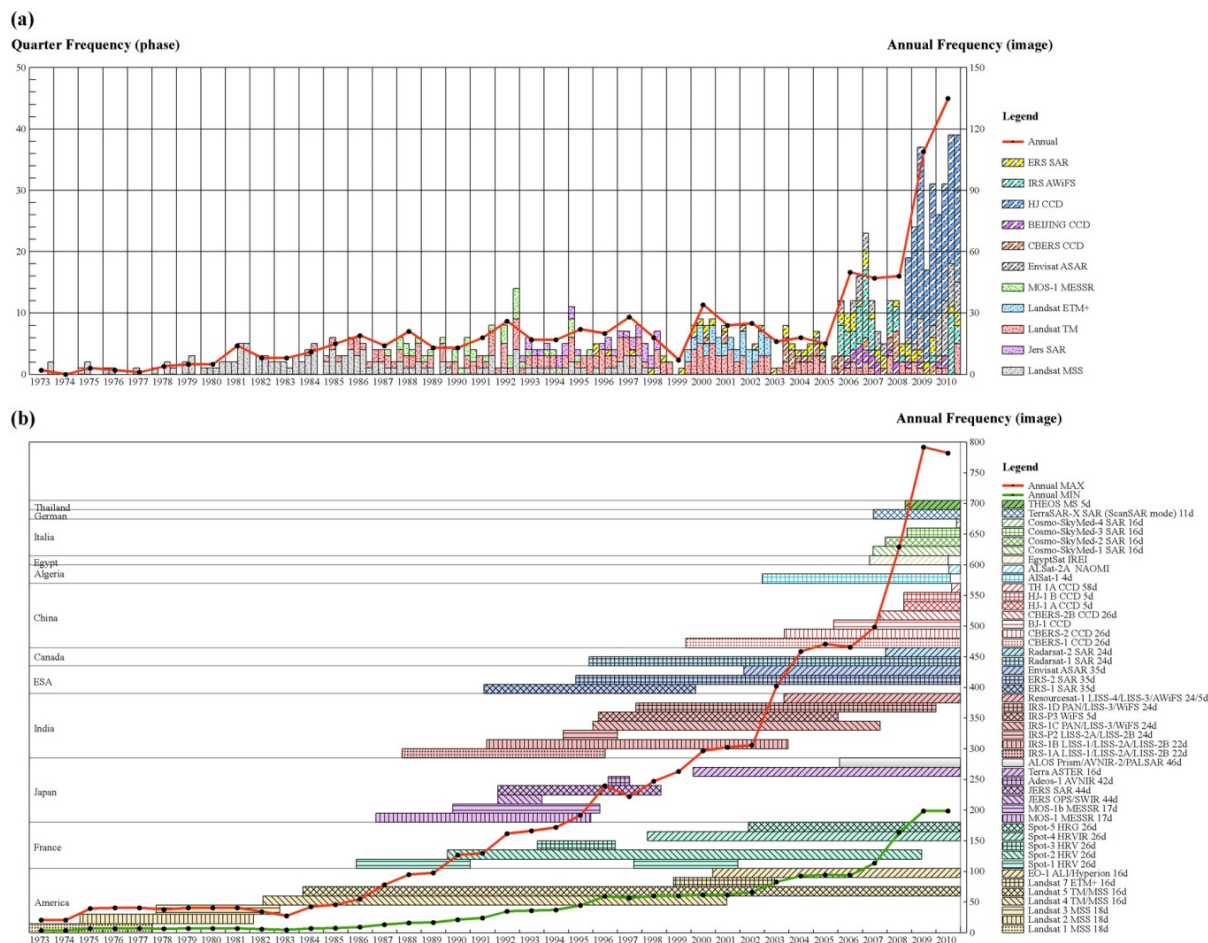

In the availability analysis of the archive satellite images described above, some satellite-image sources were not included for several reasons: (1) images taken by the SPOT series satellites were not included, because at least three scene images are needed to completely cover the middle Jiangsu coast; (2) images taken by the ASTER sensor on the Terra satellite were not included, because the ASTER images are mainly collected based on user-demand and lack routinely archived data; (3) other SAR images, including images taken by TerraSAR-X, ALOS, RADARSAT-1/2 and Cosmo-SkyMed, were not included, because these images are too expensive or difficult to access in China. The temporal resolution of the tidal flat DEMs may depend to a large degree on the number of available high-quality satellite images. Hence, we counted approximately 47 medium-resolution civilian satellite sensors (spatial resolution between 10 m and 100 m) that had been launched between 1972 and 2013 (Figure 6b) that could be used to estimate the upper limit of the temporal resolution of the tidal flat DEM based on the waterline method. In Figure 7b, the horizontal bars present the service time of the medium-resolution satellites. The red line indicates the annual sum of the available satellite images, which was estimated based on each satellite's revisiting cycle. According to [16], 16.72% of the 8,163

MODIS images taken by Terra and Aqua between 2000 and 2008 over the Jiangsu coast are of high-quality. The availability of SAR scenes for the waterline method is approximately 60% [12,32, 33]. Hence, the availability rate of high-quality satellite images was set to this proportion for the optical images, and the availability rate for the SAR images was 60%. The green line in Figure 7b represents the potential annual sum of available high-quality satellite images. If all of these potential medium-resolution satellite images are taken into account, the upper limit of the temporal resolution of the tidal flat DEM based on the waterline method should be improved significantly, due to the increase in the number of sensors; the temporal resolution increases to one year since 1993 (more than 50 images per year), half a year since 2004 (more than 100 images per year) and three months since 2009 (more than 200 images per year). This increased temporal resolution makes it feasible to conduct research on the inter-annual, inter-seasonal or, even, intra-seasonal trends of tidal flat evolution. In the future, this method may be able to detect short-term terrain changes caused by a single storm surge with the continued launching of more earth observation satellites.

Figure 8. Tidal flat DEMs of the Dongsha Sandbank over different periods: (**a**) 1973–1977; (**b**) 1980–1981; (**c**) 1990–1991; (**d**) 2000–2001; (**e**) 2006; (**f**) 2008; (**g**) spring, 2009 (March to May 2009); and (**h**) winter, 2009 (December 2009 to February 2010).
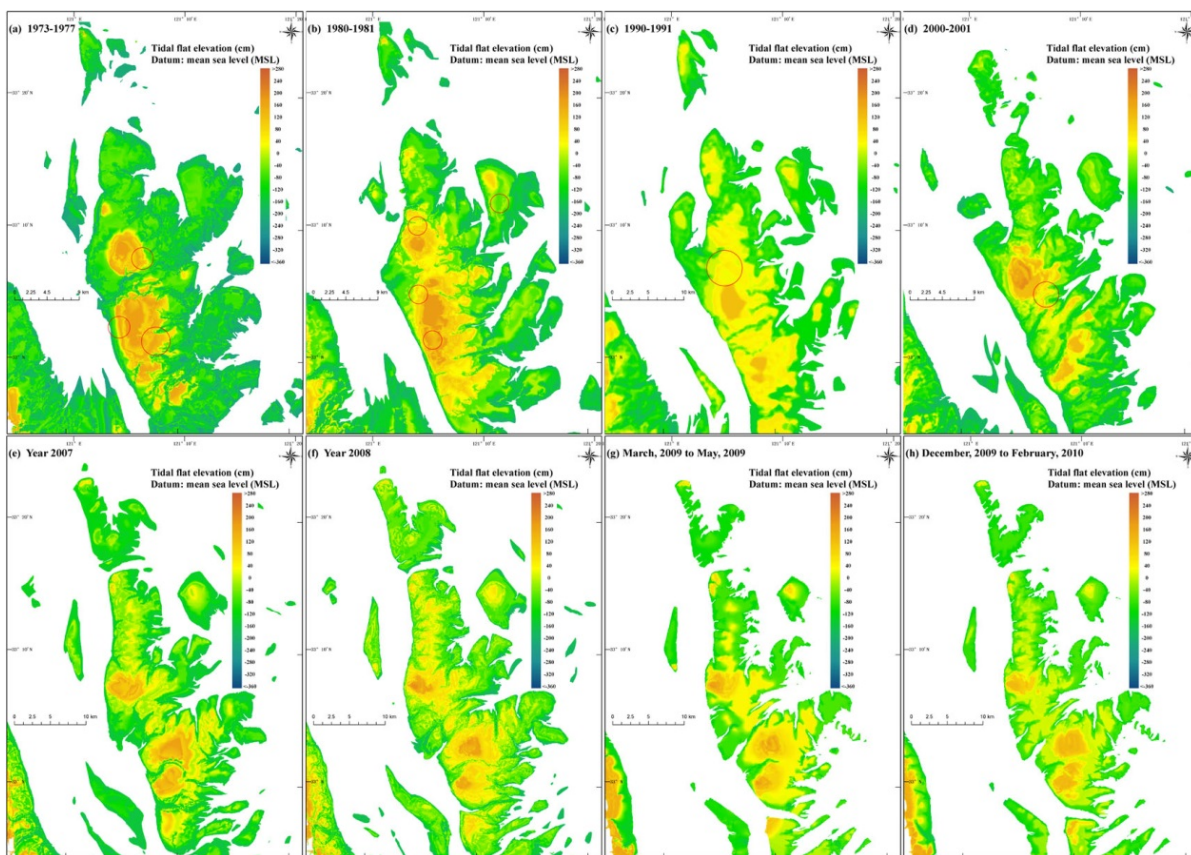
To demonstrate the ability to construct periodic tidal flat DEMs for the past several decades, eight phases of tidal flat DEMs of the Dongsha Sandbank at four temporal resolutions (four years, two years, one year and three months) (Figures 8a–h) were constructed using the aforementioned method. The DEMs are based on 15 images (1973–1977; the time span of the 15 images is 1,431 days, hereinafter

denoted as d), 18 images (1980–1981; 603 d), 22 images (1990–1991; 640 d), 26 images (2000; 312 d), 27 images (2007; 342 d), 29 images (2008; 355 d), 29 images (March to May 2009; 81 d) and 25 images (December 2009 to February 2010; 80 d) (Table 2). All of the important topographic features, such as sandbanks and tidal channels, can be identified and are positioned precisely on these maps. Note that the results for the first three phases of tidal flat DEMs are marginally satisfactory: in general, the elevation in the Dongsha Sandbank always decreases from the center to the margin, but some unnatural ripples are present near the center of the sand ridge in the resultant DEMs (red circles in Figures 8a–d). These features are primarily attributed to the long time span. However, these three phases of tidal flat DEMs based on the waterline method may be the sole topographical data available for tidal flat evolution trend analysis over the past decades. Three interesting phenomena can be observed from the eight phases of DEMs of the Dongsha Sandbank over the past 40 years: (1) the area of the exposed sandbanks decreased from 1973 to 2010; (2) the northern small sandbank had a southward movement tendency; and (3) the western margin of the Dongsha Sandbank was straight during the twentieth century, then became more curvy over the first ten years of this century. These findings agree with field observations. However, the evolutionary trend of the Dongsha Sandbank is not the main focus of this paper; the trends observed from the eight tidal DEMs were presented as circumstantial evidence to illustrate the feasibility of building DEMs of tidal flats from previous decades based on satellite images despite the lack of synchronous ground data.

5. Conclusions

This research quantitatively analyzed the relationship between the accuracy of DEMs that are based on the waterline method and the controlling factors. The three major conclusions of the study are as follows:

(1) The number of satellite images used in the waterline method and the coverage rate of the waterline points are statistically correlated with the RMSEs of the resultant DEMs. In particular, the coverage rate of the waterline points is more closely related to the accuracy of the resultant DEMs than the number of images, which implies that increasing the number of satellite images used in the waterline method may only slightly improve the accuracy, while additional waterline points could significantly improve the accuracy of the DEMs.

(2) The area and the slope of the tidal flats reflect the inherent spatial variability of the tidal flats. Tidal flat DEM inversion over a large-scale tidal flat with complex landforms requires denser waterlines and a higher coverage rate to delineate the micro-morphology and to account for regional loss.

(3) The availability analysis of the archive satellite images indicated that the waterline method is able to recover tidal flat terrains from the past forty years. The upper limit of the temporal resolution of the tidal flat DEMs is one year since 1992, half a year since 2004 and three months since 2008, which makes the method practical for research on inter-annual, inter-seasonal or even intra-seasonal trends of tidal flat evolution.

Acknowledgments

Conflicts of Interest

The authors declare no conflict of interest.

References and Notes

1. Chen, J.Y.; Cheng, H.Q.; Dai, Z.J.; Eisma, D. Harmonious development of utilization and protection of tidal flats and wetlands—A case study in Shanghai area. *China Ocean Eng.* **2008**, *22*, 649–662.
2. Wang, Y.P.; Gao, S.; Jia, J.J.; Thompson, C.E.L.; Gao, J.H.; Yang, Y. Sediment transport over an accretional intertidal flat with influences of reclamation, Jiangsu coast, China. *Mar. Geol.* **2012**, *291*, 147–161.
3. Murray, N.J.; Phinn, S.R.; Clemens, R.S.; Roelfsema, C.M.; Fuller, R.A. Continental scale mapping of tidal flats across East Asia using the Landsat archive. *Remote Sens.* **2012**, *4*, 3417–3426.
4. Wimmer, C.; Siegmund, R.; Schwabisch, M.; Moreira, J. Generation of high precision DEMs of the Wadden Sea with airborne interferometric SAR. *IEEE Trans. Geosci. Remote Sens.* **2000**, *38*, 2234–2245.
5. Klemas, V. Beach profiling and LIDAR bathymetry: An overview with case studies. *J. Coast. Res.* **2011**, *27*, 1019–1028.
6. Sallenger, A.H.; Krabill, W.B.; Swift, R.N.; Brock, J.; List, J.; Hansen, M.; Holman, R.A.; Manizade, S.; Sontag, J.; Meredith, A.; *etc*. Evaluation of airborne topographic lidar for quantifying beach changes. *J. Coast. Res.* **2003**, *19*, 125–133.
7. Mason, D.C.; Gurney, C.; Kennett, M. Beach topography mapping: A comparison of techniques. *J. Coast. Conserv.* **2000**, *6*, 113–124.
8. Durbha, S.S.; King, R.L. Semantics-enabled framework for knowledge discovery from earth observation data archives. *IEEE Trans. Geosci. Remote Sens.* **2005**, *43*, 2563–2572.
9. Li, Y.K.; Bretschneider, T.R. Semantic-sensitive satellite image retrieval. *IEEE Trans. Geosci. Remote Sens.* **2007**, *45*, 853–860.
10. Mason, D.C.; Amin, M.; Davenport, I.J.; Flather, R.A.; Robinson, G.J.; Smith, J.A. Measurement of recent intertidal sediment transport in Morecambe Bay using the waterline method. *Estuar. Coast. Shelf Sci.* **1999**, *49*, 427–456.

11. Mason, D.C.; Davenport, I.J.; Flather, R.A.; Gurney, C. A digital elevation model of the inter-tidal areas of the Wash, England, produced by the waterline method. *Int. J. Remote Sens.* **1998**, *19*, 1455–1460.

12. Heygster, G.; Dannenberg, J.; Notholt, J. Topographic mapping of the German tidal flats analyzing SAR images with the waterline method. *IEEE Trans. Geosci. Remote Sens.* **2010**, *48*, 1019–1030.

13. Anthony, E.J.; Dolique, F.; Gardel, A.; Gratiot, N.; Proisy, C.; Polidori, L. Nearshore intertidal topography and topographic-forcing mechanisms of an Amazon-derived mud bank in French Guiana. *Cont. Shelf Res.* **2008**, *28*, 813–822.

14. Baghdadi, N.; Gratiot, N.; Lefebvre, J.P.; Oliveros, C.; Bourguignon, A. Coastline and mudbank monitoring in French Guiana: Contributions of radar and optical satellite imagery. *Can. J. Remote Sens.* **2004**, *30*, 109–122.

15. Liu, Y.X.; Li, M.C.; Cheng, L.; Li, F.X.; Chen, K.F. Topographic mapping of offshore sandbank tidal flats using the waterline detection method: A case study on the Dongsha Sandbank of Jiangsu Radial Tidal Sand Ridges, China. *Mar. Geod.* **2012**, *35*, 362–378.

16. Liu, Y.X.; Li, M.C.; Cheng, L.; Li, F.X.; Shu, Y.M. A DEM inversion method for inter-tidal zone based on MODIS dataset: A case study in the Dongsha Sandbank of Jiangsu Radial Tidal Sand-Ridges, China. *China Ocean Eng.* **2010**, *24*, 735–748.

17. Liu, Y.X.; Li, M.C.; Mao, L.; Cheng, L.; Li, F.X. Toward a method of constructing tidal flat digital elevation models with MODIS and medium-resolution satellite images. *J. Coast. Res.* **2013**, *29*, 438–448.

18. Lohani, B.; Mason, D.C. Construction of a digital elevation model of the Holderness coast using the waterline method and airborne thematic mapper data. *Int. J. Remote Sens.* **1999**, *20*, 593–607.

19. Niedermeier, A.; Hoja, D.; Lehner, S. Topography and morphodynamics in the German Bight using SAR and optical remote sensing data. *Ocean Dyn.* **2005**, *55*, 100–109.

20. Zhao, B.; Guo, H.; Yan, Y.; Wang, Q.; Li, B. A simple waterline approach for tidelands using multi-temporal satellite images: A case study in the Yangtze Delta. *Estuar. Coast. Shelf Sci.* **2008**, *77*, 134–142.

21. Ren, M.E. The South Yellow Sea Radial Sand Ridges (SYSRSR). In *Investigation Report on Jiangsu Tidal Flat and Tidal Resources* (In Chinese); China Ocean Press: Beijing, China, 1985; pp. 164–168.

22. Zhang, R.S.; Chen, C.J. The Distribution of Modern Offshore Sandbanks in Jiangsu. In *Study of the Evolution of Jiangsu Offshore Sandbanks and the Prospects for Tiaozini Sandbanks Merging into Land* (In Chinese); China Ocean Press: Beijing, China, 1992; pp. 23–25.

23. Zhang, R.S. Equilibrium state of tidal mud flat, a case-coastal area of central Jiangsu, China. *Chin. Sci. Bull.* **1995**, *40*, 1363–1368.

24. Zhang, R.S.; Shen, Y.M.; Lu, L.Y.; Yan, S.G.; Wang, Y.H.; Li, J.L.; Zhang, Z.L. Formation of Spartina alterniflora salt marshes on the coast of Jiangsu Province, Spain. *Ecol. Eng.* **2004**, *23*, 95–105.

25. Zhang, R.S. Suspended sediment transport processes on tidal mud flat in Jiangsu Province, China. *Estuar. Coast. Shelf Sci.* **1992**, *35*, 225–233.

26. Ren, M.E.; Zhang, R.S.; Yang, J.H. Effect of typhoon No.8114 on coastal morphology and sedimentation of Jiangsu Province, People's Republic of China. *J. Coast. Res.* **1985**, *1*, 21–28.

27. Japan Aerospace Exploration Agency. Available online: http://www.eorc.jaxa.jp (accessed on 31 July 2013).

28. China Remote Sensing Satellite Ground Station. Available online: http://www.rsgs.ac.cn (accessed on 31 July 2013).

29. Remote Sensing Technology Center of Japan. Available online: https://cross.restec.or.jp (accessed on 31 July 2013).

30. China Centre for Resources Satellite Data and Application. Available online: http://www.cresda.com (accessed 31 July 2013).

31. Beijing Twenty-first Century Science and Technology Development Co., L.B. Available online: http://www.blmit.com.cn (accessed on 31 July 2013).

32. Mason, D.C.; Davenport, I.J.; Robinson, G.J.; Flather, R.A.; McCartney, B.S. Construction of an intertidal digital elevation model by the "water-line" method. *Geophys. Res. Lett.* **1995**, *22*, 3187–3190.

33. Chen, L.C.; Rau, J.Y. Detection of shoreline changes for tideland areas using multi-temporal satellite images. *Int. J. Remote Sens.* **1998**, *19*, 3383–3397.

34. Ryu, J.H.; Won, J.S.; Min, K.D. Waterline extraction from Landsat TM data in a tidal flat—A case study in Gomso Bay, Korea. *Remote Sens. Environ.* **2002**, *83*, 442–456.

35. Ryu, J.-H.; Kim, C.-H.; Lee, Y.-K.; Won, J.-S.; Chun, S.-S.; Lee, S. Detecting the intertidal morphologic change using satellite data. *Estuari. Coast. Shelf Sci.* **2008**, *78*, 623–632.

36. Chen, K.F.; Wang, Y.H.; Lu, P.D.; Zheng, J.H. Effects of coastline changes on tide system of Yellow Sea off Jiangsu coast, China. *China Ocean Eng.* **2009**, *23*, 741–750.

37. Klocke, B. *Topographische Karte des Wattenmeeres aus ERS*-1 *SAR- und Modelldaten*; Logos Verlag: Berlin, Germany, 2001; Volume 7.

38. Wang, Y. *Satellite SAR Imagery for Topographic Mapping of the Tidal Flat Areas in the Dutch Wadden Sea*; ITC Enschede: Enschede, The Netherlands, 1997; Volume 47.

39. Mason, D.C.; Davenport, I.J.; Flather, R.A.; Gurney, C.; Robinson, G.J.; Smith, J.A. A sensitivity analysis of the waterline method of constructing a digital elevation model for intertidal areas in ERS SAR scene of eastern England. *Estuar. Coast. Shelf Sci.* **2001**, *53*, 759–778.

40. Blott, S.J.; Pye, K. Application of lidar digital terrain modelling to predict intertidal habitat development at a managed retreat site: Abbotts Hall, Essex, UK. *Earth Surf. Process. Landf.* **2004**, *29*, 893–905.

41. Mason, D.C.; Scott, T.R.; Dance, S.L. Remote sensing of intertidal morphological change in Morecambe Bay, UK, between 1991 and 2007. *Estuar. Coast. Shelf Sci.* **2010**, *87*, 487–496.

42. Liu, Y.; Li, M.; Mao, L.; Cheng, L.; Chen, K. Seasonal pattern of tidal-flat topography along the Jiangsu middle coast, China, using HJ-1 optical images. *Wetlands* **2013**, *33*, 871–886.